Check for updates

On the Response Speed of Narrowband Organic Optical Upconversion Devices

Wei-Hsu Hu, Camilla Vael, Matthias Diethelm, Karen Strassel, Surendra B. Anantharaman, Abdessalem Aribia, Marco Cremona, Sandra Jenatsch, Frank Nüesch, and Roland Hany*

Organic upconversion devices (OUCs) consist of an organic infrared photodetector and an organic visible light-emitting diode (OLED), connected in series. OUCs convert photons from the infrared to the visible and are of use in applications such as process control or imaging. Many applications require a fast OUC response speed, namely the ability to accurately detect in the visible a rapidly changing infrared signal. Here, high image-contrast, narrowband OUCs are reported that convert near-infrared (NIR) light at 980 and 976 nm with a full-width at half maximum of 130 nm into visible light. Transient photocurrent measurements show that the response speed decreases when lowering the NIR light intensity. This is contrary to conventional organic photodetectors that show the opposite speed-versus-light trend. It is further found that the response speed increases (when using a phosphorescent OLED) or decreases (for a fluorescent OLED) when increasing the driving voltage. To understand these surprising results, an analysis by numerical simulation is conducted. Results show that the response speed behavior is primarily determined by the electron mobility in the OLED. It is proposed that the low electron drift velocity in the emitter layer sets a fundamental limit to the response speed of OUCs.

1. Introduction

Efficient wavelength-selective sensing and imaging of near-infrared (NIR) light is critical to fiber-optical communication, optical sensors, medical imaging, robotics, or machine vision systems.[1–7] Currently, NIR imaging is realized with inorganic photodetector arrays interconnected with a silicon readout circuit.[2,3,8] However, such cameras are difficult to manufacture

and are still cost prohibitive for most consumer and low-end applications. In addition, due to the broadband absorption of inorganic semiconductors, spectrally selective detection is not possible without attached optical filters.

As an alternative approach, optical upconversion devices have been developed that directly convert NIR light into visible light. These devices are also denoted as upconversion photodetector,[9] upconversion display/imager,[10,11] or upconversion light-emitting diode.[12] The basic idea of any upconverter is the serial connection of a NIR photodetector with a visible light-emitting component. When NIR light is absorbed in the photodetector, a current is generated and directly converted into a visible image by the emitter element. Important advantages of this design concept are that no intermediate electronics for data processing and no external display for data visualization are required. We note that the functionality of an upconverter is different from the several known photon upconversion processes. Photon upconversion is a process that converts sequentially absorbed photons of low energy into a photon of higher energy.

All-organic upconversion devices (OUCs) are composed of an organic NIR photodetector and an organic light-emitting diode (OLED). OUCs can be fabricated entirely from solution over large area using coating and printing processes. This potentially enables new and alternative NIR imaging applications

W.-H. Hu, M. Diethelm, K. Strassel, S. B. Anantharaman, F. Nüesch, R. Hany
Laboratory for Functional Polymers
Swiss Federal Laboratories for Materials Science and Technology (Empa)
Dübendorf 8600, Switzerland
E-mail: roland.hany@empa.ch

W.-H. Hu, C. Vael, M. Diethelm, K. Strassel, S. B. Anantharaman, F. Nüesch
Institute of Materials Science and Engineering
Ecole Polytechnique Fédérale de Lausanne (EPFL)
Station 12, Lausanne 1015, Switzerland

C. Vael, S. Jenatsch
Fluxim AG
Katharina-Sulzer-Platz 2, Winterthur 8400, Switzerland

A. Aribia
Thin Films and Photovoltaics
Swiss Federal Laboratories for Materials Science and Technology (Empa)
Dübendorf 8600, Switzerland

M. Cremona
Optoelectronic Molecular Laboratory
Physics Department
Pontifical Catholic University of Rio de Janeiro (PUC-Rio)
Rio de Janeiro 224543-970, Brazil

with wearable and flexible devices. A further advantage of OUCs is that a high image resolution (e.g., ≈430,[11,13,14] 1588[15] dots per inch) can be achieved without pixelation of the active layer. This is because of the poor lateral conductivity and thin thickness of the organic layers, which suppresses lateral current spreading in OUCs.

The state-of-the-art of the research on OUCs until 2018 is summarized in ref. [16] Since then, research efforts were directed to extend the detection into the shortwave infrared range, i.e., beyond 1000 nm,[11,12,17,18] or to improve important device figures of merit, such as lowering the operating voltage or improving the NIR light sensitivity.[10,14,15]

Current OUCs use broadband NIR-selective or panchromatic photodetectors, but true narrowband OUCs with a spectral NIR response of typically below 150 nm[1] full-width at half-maximum (FWHM) have not been presented. In principle, narrowband selectivity with panchromatic absorbers[20,21] can be achieved with optical filters or by using various filter-free wavelength selective photo detection approaches,[2,22] such as charge collection narrowing (CCN).[4] The CCN approach is to use very thick organic films (several μm) in which the response is narrowed to the absorption onset, leading to visible blind and tuneable red and NIR narrowband response. However, when integrated in an OUC, CCN-photodetectors will completely absorb the visible emitted light. Consequently, the upconverted light must be measured at the opposite side of the incident NIR light. This requires a transparent top electrode, which complicates the device fabrication process. The same is true when using optical filters in the visible.

Here, we achieve NIR narrowband (FWHM 130 nm) photodetection with a heptamethine J-aggregated polymethine cyanine dye. Polymethine dyes have a single maximum absorption in the NIR but they cannot be designated as true narrowband absorbers because FWHM absorptions are well over 100 nm, especially when dyes are processed into a film.[18,23,24] We exploit the fact that polymethine dyes can self-assemble into highly ordered (J- or H-)aggregated nanostructures.[25,26] The formation of J-aggregates results in a redshift (typically 50–100 nm[27]) and narrowing of the absorption band compared to the monomer, which has already been exploited by us and others for NIR narrowband polymethine photodetectors.[28–31]

By combining the cyanine J-aggregate photodetector with a fluorescent or phosphorescent OLED, OUCs were obtained that convert NIR photons most efficiently at 980 or 976 nm to visible yellow or green photons. Our OUCs are characterized by very low dark current values, which results in a high NIR light on/off ratio of the luminance and a high image contrast. We measure the transient photocurrent response, both as a function of the light intensity and the applied bias voltage. The response speed of OUCs is a crucial parameter for imaging applications, as it sets the frame rate for image generation. We find that the response speed slows down when lowering the NIR light intensity, and either increases (when using the phosphorescent OLED) or decreases (when using the fluorescent OLED) with increasing voltage. To understand these unexpected results, we carry out an analysis by numerical drift-diffusion modeling. Simulation results show that the OUC response speed is governed by an intricate interplay between the charge mobility values in the different layers and that, for example, an increase of the applied bias voltage does not necessarily increase the response speed, as would intuitively be taken for granted.

2. Results and Discussion

2.1. Experimental

The materials used for fabricating the OUCs and the device architectures are shown in **Figure 1**. We used a fluorescent poly(para-phenylene vinylene) copolymer (Super Yellow, SY)-based OLED or a host–guest phosphorescent Ir(ppy)$_3$ OLED. Both in the dark (no NIR light) and the on-state (in the presence of NIR light) a voltage bias is applied (**Figure 2**a). In the dark, TiO$_2$ reduces hole injection at the indium tin oxide (ITO) anode, whereas QUPD blocks electrons from flowing through the device. This suppresses the dark current, results in a high on/off ratio and a high image contrast.

We used a recently reported[29] NIR photodetector that consists of a TiO$_2$ electron transport layer on ITO that is sensitized by a near-infrared absorbing J-aggregated cyanine dye (Jcy).[28] The cyanine monomer in solution absorbs at 793 nm (Figure S1, Supporting Information), but when coated from the solvent 2,2,2-tri-fluoroethanol, the dye forms a compact and dense J-aggregate layer that absorbs at 995 nm with a narrow FWHM absorption of 52 nm (Figure 2b). The photodetector in the configuration ITO/TiO$_2$/Jcy/MoO$_3$/Ag is fairly stable, fast-responding (3 dB cut-off frequency = 50 kHz), and reaches an external quantum efficiency (EQE) at 990 nm of 12% at −2 V. Performance metrics of the photodetector are summarized in Figure S1 (Supporting Information).

The cross-linkable QUPD layer was spin-coated from toluene directly on the J-aggregate layer. This was possible because the cyanine dye is soluble in water, but insoluble in common organic solvents. We found that a single layer of QUPD is not completely compact, and the dye was partly dissolved when a TiO$_2$/Jcy/QUPD layer was rinsed with water. Therefore, to realize a more compact QUPD layer, a second film was coated on top of the first cross-linked layer. The two-layer QUPD film suppressed the dark current substantially, and the dark luminance decreased by a factor 10 (Figure S2, Supporting Information).

In the on-state, NIR light (using a 980 nm laser, 49 mW cm^{-2}) is absorbed by the Jcy layer and charge generation takes place. Electrons are extracted via TiO$_2$ at the ITO anode, while holes drift via the QUPD layer in the OLED where they recombine with electrons injected from the cathode under the emission of visible light (Figure 2a). The electroluminescence spectra of the two OUCs are shown in Figure 2b. Because we used a non-transparent aluminum top electrode, the visible light leaves the device at the side of the incident NIR light source. When using a panchromatic NIR photodetector, a fraction of the emitted visible light would be reabsorbed when passing through the photodetector. In our case, however, the transmission of the full layer stack is over 85% at the wavelengths where SY and Ir(ppy)$_3$ emit, and reabsorption of emitted light is small.

Luminance–voltage and current–voltage characteristics of the SY-OUCs are shown in **Figure 3**a. The reproducibility of
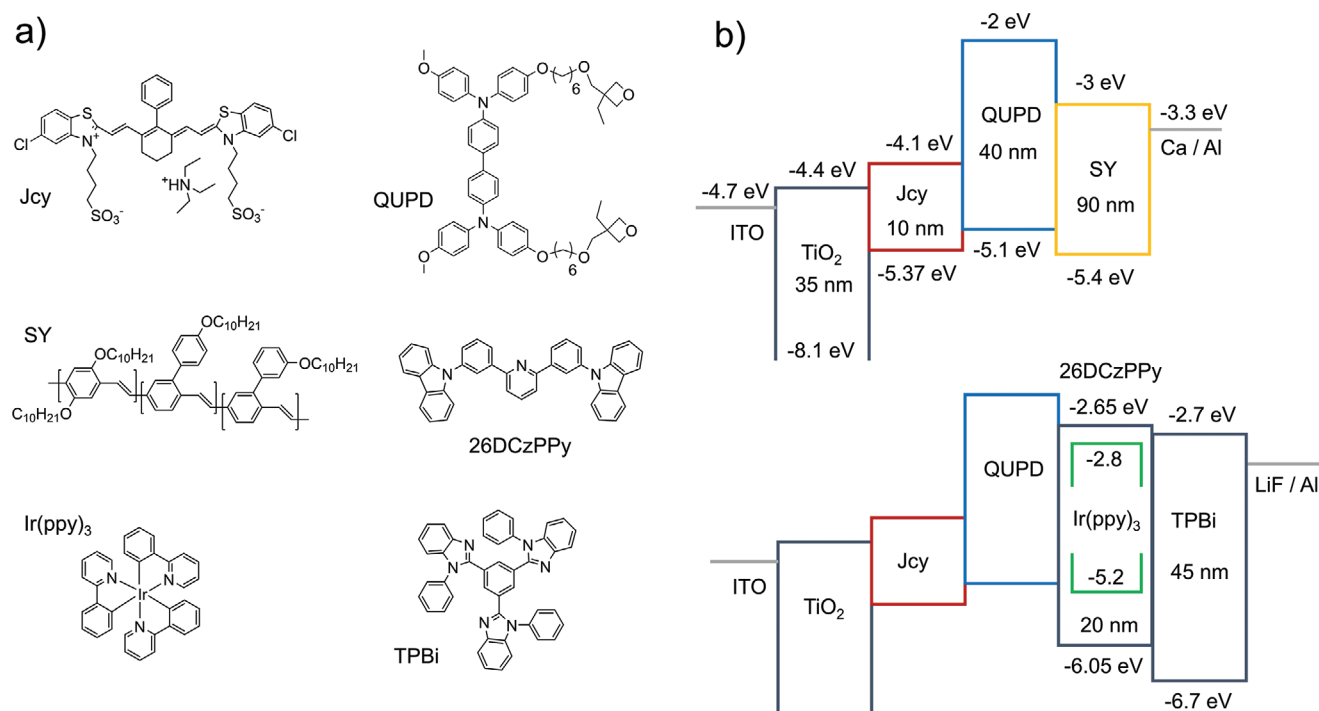
Figure 1. a) Chemical structures of the compounds used in this study. b) OUC stacks with a fluorescent Super Yellow (SY) or a phosphorescent host–guest OLED as visible light-emitting component.

device fabrication is shown in Figure S3 (Supporting Information). The dark current is very small and reaches 0.7 mA cm^{-2} at 12 V. Up to 8 V, the dark luminance is at the detection limit (0.01 cd m^{-2}) of our luminance meter, and reaches around 0.27 cd m^{-2} at 12 V. When replacing the sol–gel derived TiO$_2$ with a more dense TiO$_2$ layer grown via atomic layer deposition,

the dark current was suppressed further by a factor of 8 and the dark luminance remained at 0.01 cd m^{-2} out to 10 V (Figure S4, Supporting Information).

In the presence of NIR light, the device turn-on is at 3.5 V (1 cd m^{-2}) and the maximum on/off ratio for the luminance is 8300 at 8 V. In the case of facile electron injection from the
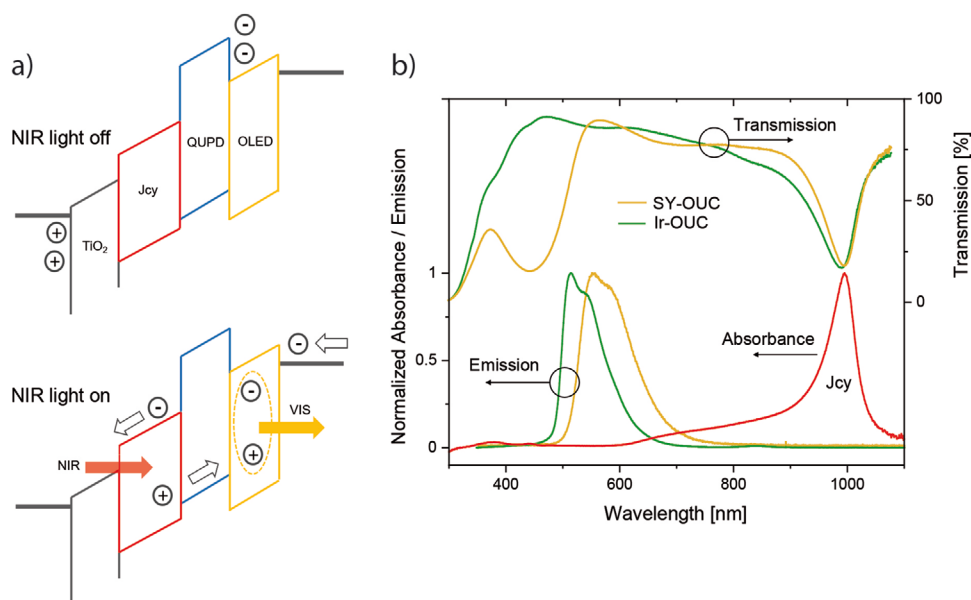

Figure 2. a) Schematic functionality of the OUC in the absence and presence of NIR light. b) Absorbance spectrum (red line) of the aggregated Jcy cyanine dye film on TiO$_2$ and experimental emission spectra of OUCs containing the SY- and Iridium-based OLED. Also included are the experimental transmission spectra of the full OUC stacks, next to the top electrode. Line colors are orange for SY-OUC and green for Ir-OUC.
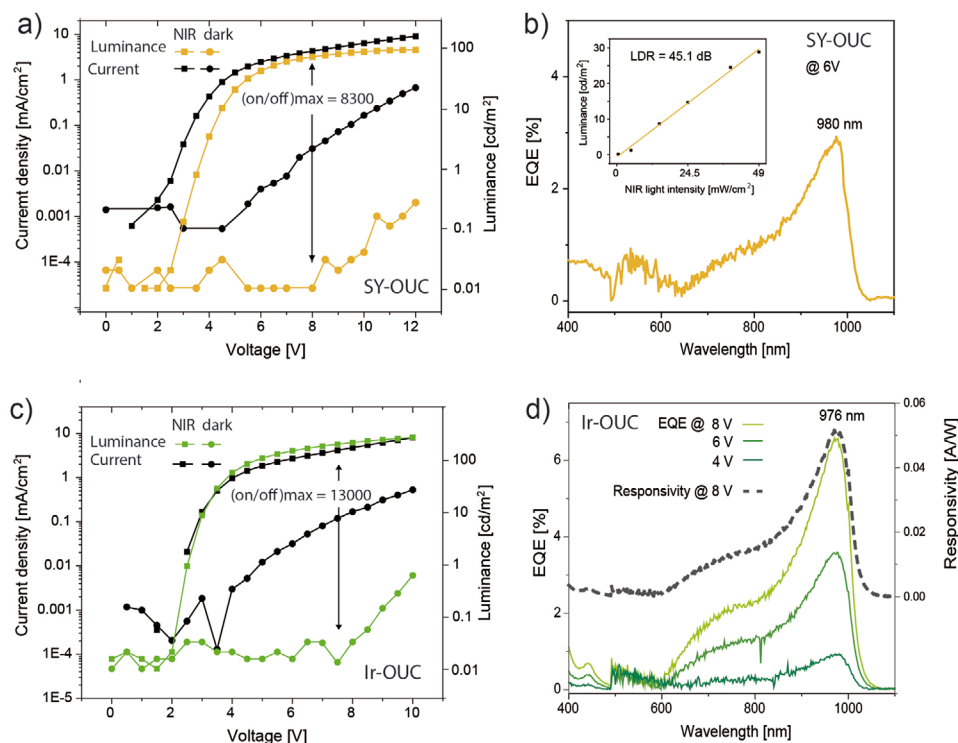
Figure 3. a,c) Performance characteristics of OUCs with and without NIR light using a fluorescent (a) or phosphorescent (c) OLED. b) EQE of the SY-OUC. The inset shows the linear dynamic range (LDR) of the NIR light-induced luminance, evaluated at a voltage of 6 V. d) EQE of the Ir-OUC as function of voltage bias and responsivity curve at 8 V.

cathode, the current in the on-state is limited by the number of photogenerated holes in the photodetector and therefore is expected to level off at high voltages. Because the EQE of our photodetector increases with bias (Figure S1, Supporting Information), we do not observe a clear saturation trend, and the current and luminance increase continuously with increasing voltage.

The current efficacy of the SY-OUC in the on-state is lower than expected. The maximum efficacy is 2.7 cd A^{-1} at 6 V, much below the value of 12.6 cd A^{-1} we measured for an ITO/QUPD/SY/Ca/Al OLED (Figure S5, Supporting Information). This is in line with the calculated ratio between the numbers of visible emitted photons to impinging NIR photons, the photon-to-photon conversion efficiency (P2PCE).[32] P2PCE was 0.16% at 10 V. The P2PCE can also be approximated from the individual EQEs of the photodetector (EQE ≈ 10%) and the OLED (EQE = 2.89%).[33,34] The value for the approximated P2PCE is EQE(photodetector) × EQE(OLED) ≈ 0.1 × 2.89% = 0.29%, which is about a factor of two higher than the experimental value. From simulation results (see below), we take the low current efficacy as the result of exciton quenching in the emitter layer because the charge recombination zone is very narrow and close at the QUPD-SY interface. To move the recombination zone away from this interface, we experimentally inserted an additional hole-transporting MoO$_3$ (15 nm) layer between QUPD and SY. Thereby, the current efficacy increased strongly to 8.3 cd A^{-1} (Figure S5, Supporting Information). From preliminary long-term experiments, we also find that a recombination zone close to the QUPD-SY

interface compromises the device stability (Figure S5, Supporting Information).

Figure 3b shows the EQE spectrum for the SY-OUC at a voltage bias of 6 V, spectra for other voltages are shown in Figure S3 (Supporting Information). In contrast to the absorption of the neat Jcy film (maximum absorption at 995 nm, FWHM 52 nm), the maximum EQE (2.9%, responsivity 22.9 mA W^{-1}) is at 980 nm and the EQE peak is relatively broader (FWHM 130 nm). We ascribe this broadening of the EQE peak to optical interference effects (weak microcavity) because the absorbing layer is sandwiched between a strongly (Al) and weakly (glass/ITO) reflecting interface.[18,28,34] The EQE falls off toward shorter wavelengths but is well below 1% between 400 and 700 nm. This means that the response of the SY-OUC to visible (background) light is very small.

The inset of Figure 3b shows the response of the luminance when varying the NIR light intensity. The linear dynamic range (LDR) describes the range within which the upconverted luminance scales linearly with the NIR light intensity (at 980 nm). We varied the NIR light intensity from 49 to 0.49 mW cm^{-2} and measured corresponding luminance values of 28.8 and 0.16 cd m^{-2}. The maximum NIR light intensity was fixed by our NIR laser source, and to avoid overestimation of the lower luminance level,[15] we did not decrease the NIR light intensity further. With these values, the calculated LDR is at least 45 dB (see the Experimental Section).

Luminance and current versus voltage trends for the Ir-OUC are shown in Figure 3c; and Figure S3 (Supporting Information). Compared to the SY-OUC, the device turn-on voltage

is lowered to 2.5 V, and because of the higher efficiency of the phosphorescent OLED (Ir-OUC maximum 5.7 cd A^{-1} at 6 V, P2PCE = 0.53%), the maximum on/off luminance ratio increases to 13 000. However, especially the dark luminance of the Ir-OUC is higher than for the SY-OUC (0.2 cd A^{-1} vs 0.03 at 10 V). This can be explained by an increased hole dark current in the Ir-OUC. The hole barrier at the QUPD-SY interface is around 0.3 eV (Figure 1b), whereas the energy barrier for hole injection from QUPD to the Ir(ppy)$_3$ guest is only around 0.1 eV. Holes that enter the OLED can radiatively recombine with electrons that are injected in the emitter layer already in the dark and that pile up at the QUPD-OLED interface (see Simulation results, below).

Figure 3d shows EQE spectra of the Ir-OUC as function of the voltage bias. The maximum EQE at 976 nm is slightly shifted compared to the SY-OUC, but the FWHM (130 nm) is the same. The peak EQE increased superlinear with voltage and was 0.9% at 4 V, 3.6% at 6 V, and 6.6% at 8 V. First, the EQE increase of the OUC with bias is because the EQE of our photodetector increases with bias. In addition, the EQE increases because of the energetic barrier for hole carrier transport in the Ir-OUC that can be effectively overcome when the electric field is increased. The LDR for the Ir-OUC is at least 46.7 dB (Figure S3, Supporting Information).

We evaluated the response time of the OUCs by transient photocurrent response measurements. The speed of response is related to the time it takes to generate charges after the light stimulus, to extract the photogenerated electrons at the anode and to transport the holes into the emissive layer, where they recombine with electrons that are injected at the cathode and transported through the emissive layer to the recombination zone. For our OUCs, we measured resistance-capacitance time constants of ≈50 ns, so the speed of response is not limited by the charging of the geometrical capcitance ($f_{3dB,RC}$ = 1/2πRC = 3 MHz).[35] The 3dB cut-off frequency (also referred to as bandwidth) was determined as the light modulation frequency at which the photocurrent has dropped to 0.71 of that under continuous illumination.[2,36] Parameters related to the 3 dB cut-off frequency are the rise and fall times that are commonly reported as the duration of the response to increase from 10% to 90% or to decrease from 90% to 10%.

For the Ir-OUC (**Figure 4**a, average from 4 devices), the 3 dB cut-off frequency increases when the bias voltage is increased and levels off at around 4 kHz at 10 V. This is the expected trend, because the drift velocity (v_{drift} = charge mobility x electric field) of charges gets faster by an enhanced electric field.[1] For the SY-OUC, however, we observe a different behavior (Figure 4b). First, the response speed is much lower than measured for the Ir-OUC. Second, the response speed first slightly increases with voltage (or stays almost constant, Figure S6, Supporting Information), but afterward decreases by about a factor of five. The inset of Figure 4b shows that the rise time of the current response at 6 V is clearly shorter than at 10 V, which confirms the response speed measurement in the frequency domain. We observed a further decrease of the response speed during device stressing. Therefore, a SY-OUC was kept
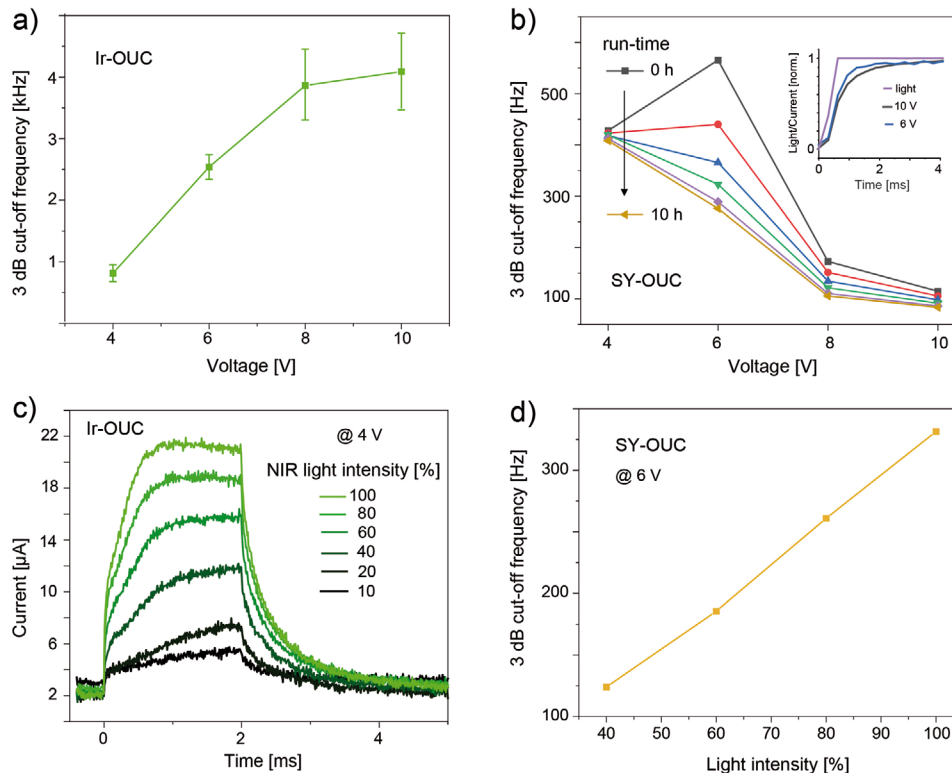

Figure 4. a,b) Speed of response under pulsed NIR illumination (950 nm) as function of voltage and c,d) as function of light intensity for Ir-OUC and SY-OUC, respectively. In (b), for the SY-OUC, the response speed was also measured during continuous device stressing over 10 h. In (c), for the Ir-OUC, the rise time clearly decreases with increasing light intensity, which indicates that the response speed slows down for lower light intensity.

at a constant voltage of 5 V and was continuously illuminated with light at 950 nm. The 3 dB cut-off frequency decreased continuously during the first 3 h of stressing (black–red–blue trends, Figure 4b) and stayed roughly constant afterward. This trend is explained by the formation of hole traps in SY during operation (see below).

The response speed was also measured as function of the NIR light intensity. Both for the Ir-OUC (Figure 4c) and the SY-OUC (Figure 4d), the response speed slows down with decreasing light intensity. Again, this is an unexpected result. For organic NIR photodetectors, the opposite trend was reported and the fall time of the transient photocurrent increased strongly with increasing charge carrier density.[37–39]

2.2. Simulation

The functionality of the OUC is governed by an intricate interplay between charge generation as well as transport and recombination in the photodetector and emission layer, for which an intuitive explanation is difficult. We resorted to an analysis by numerical modeling of the SY-OUC to gain insight into three peculiar experimental observations, namely i) the low OUC current efficacy, ii) the decrease of the response speed with increasing voltage, and iii) the decrease of the response speed with decreasing NIR light intensity, which is also observed

for the Ir-OUC. Due to the many simulation parameters involved, our goal is to capture the essential features and we do not attempt a quantitative agreement between simulation and experiment. Details of the simulation and support for the arguments we give in the following discussion are summarized in the Supporting Information.

For the simulation, the chosen energy levels are shown in Figure 1b, and the mobility values are indicated in **Figure 5**a. In the dark and when the bias voltage is above the built-in voltage, electrons are injected from the cathode into the emission layer and pile up at the QUPD-SY interface (Figure 5b). In this situation, the electric field is largely screened in SY and concentrates in the Jcy and QUPD layer (Figure 5c). In the presence of NIR light, charges are generated in the Jcy layer. A fraction of photogenerated holes and electrons recombine directly in the cyanine layer, but for larger voltages the majority of holes is driven via the QUPD layer to the QUPD-SY interface. The recombination zone between photogenerated holes and injected electrons is in SY within ≈5 nm at the QUPD-SY interface (Figure 5d). We suppose that the narrow width and location of the recombination zone provides possible explanations for the low experimental OUC current efficacy, which are related to exciton quenching. First, due to the high electron density (>10^{18} cm^{-3}, Figure 5b) present in the region where excitons are formed, exciton quenching by electron polarons can occur.[40] In addition, hole transfer through QUPD results in a fraction of
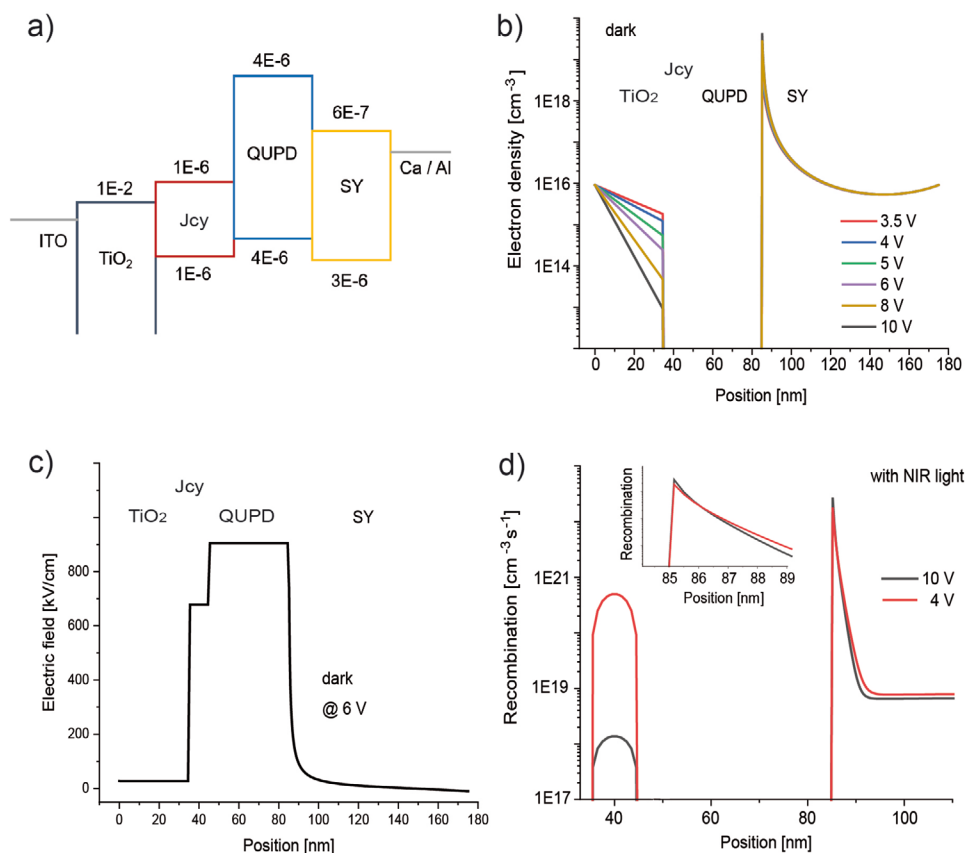

Figure 5. a) Energy level diagram used for the simulation with chosen mobility values [cm^2 V^{-1} s^{-1}] indicated. b) Electron distribution in the dark and c) corresponding electric field distribution. d) Recombination profile between electrons and holes in the presence of NIR light.
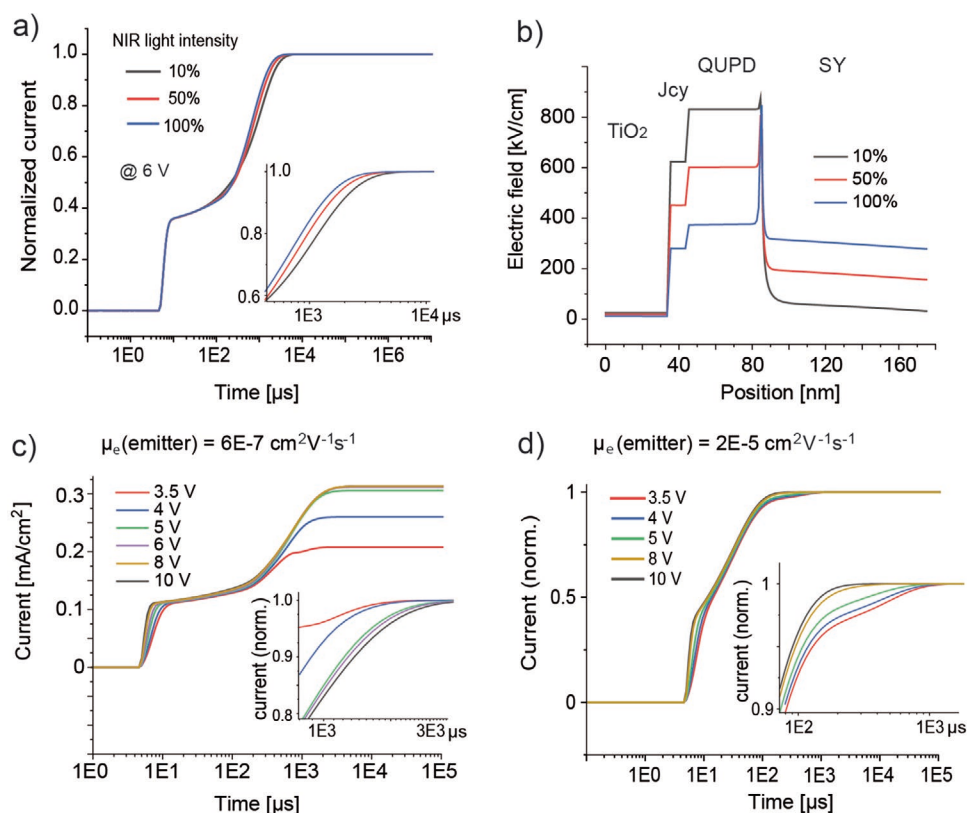
Figure 6. a) Simulation of transient currents for different NIR light intensities and b) the corresponding electric field distributions close to steady state. c,d) Simulations of transient currents as function of the applied bias voltage for c) a low and d) a high electron mobility of the emitter layer.

molecules in this layer that is oxidized. Radical cations of tetraphenylbenzidine derivatives absorb in the 400–580 nm region,[41,42] which overlaps with the emission from SY (Figure 2). Therefore, energy transfer from SY excitons to QUPD$^{+\cdot}$ is a further plausible exciton quenching mechanism, resulting in a luminance decrease.

The energy barrier (1 eV) between the lowest unoccupied molecular orbital (LUMO) levels of QUPD and SY (Figure 1b) is essential to the device functionality because it stops the electrons from flowing through the device. If this barrier is removed in the simulation, the recombination zone shifts into the QUPD layer and the calculated luminance drops almost to zero (Figure S7, Supporting Information). On the other hand, the recombination zone broadens by about 5–10 nm when the energy barrier between the highest occupied molecular orbital (HOMO) levels of QUPD and SY is removed in the simulation (Figure S8, Supporting Information). This is expected to reduce exciton quenching, because the electron polaron density is lowered and charges recombine further away from the QUPD-SY interface. Experimentally, we supported this assumption by inserting an extra MoO$_3$ layer between QUPD and SY and observed a large increase of the current efficacy (see above). Therefore, the HOMO energy barrier between the (essential) electron-blocking and the emitter material should be small, not only to ensure loss-free hole transport from the photodetector to the emitter, but also to prevent that the charge recombination zone is located next to the interface.

Figure 6a shows the simulated current transients for different NIR light intensities. The inset shows that the current reaches steady state on the order of ms and faster for higher light intensities, in agreement with the experiment (Figure 4c,d). The simulated current exhibits a very fast initial current rise, followed by a slower increase between around 100 µs and 4 ms. This current trend is also observed experimentally (Figure 4c).

The early current rise is due to the fast transport of photo-generated charges. The delayed current increase is due to a combination of hindered charge injection at the Ca-SY interface and slow electron transport ($\mu_e = 6 \times 10^{-7}$ cm^2 V^{-1} s^{-1}) from the cathode to the recombination zone, which limits the device response speed. For example, decreasing in the simulation μ_h(QUPD) or $\mu_{e,h}$(Jcy) by a factor of 10 slightly delays the early current increase, but does not influence the long-term current behavior and thereby the overall response speed (Figure S9, Supporting Information).

The only precondition in the simulation that the response speed slows down with decreasing light intensity is the low μ_e value of the emitter layer. Removal of the HOMO energy barrier between QUPD and the emitter or variations of μ_h of the emitter do not change this trend. On the other hand, if μ_e of the emitter is set to, e.g., 1×10^{-5} cm^2 V^{-1} s^{-1}, the slowdown of the current rise disappears and steady state is reached after about 200 µs. In this case, the electron transport to the recombination zone is not limiting the response speed anymore and the dependence of the response speed on the light intensity disappears in the simulation (Figures S8 and S9, Supporting Information).

While the relevant parameter (i.e., μ_e of the emitter) that determines the experimental response speed versus light

intensity trend can be pinpointed, the underlying fundamental reason for this trend is more difficult to grasp, also considering that the response speed differences are fairly small. A possible explanation can be derived from the simulated electric field distributions shown in Figure 6b. When increasing the light intensity, more charges are photogenerated. These charges travel to the anode (electrons) and to the emitter layer (holes) and thereby screen the electric field in the Jcy and QUPD layer. This effect decreases the drift velocity of photogenerated charges. At the same time, the electric field in the emitter increases with higher light intensity, which increases the speed of electrons that are transported through the emitter layer to the recombination zone. Thus, it appears that with increasing light intensity the reduction of the hole velocity in the QUPD layer is overcompensated by an increase of the electron velocity in the emitter layer, such that the overall response speed increases.

Figure 6c,d shows simulated current trends as function of the applied voltage bias. Again, the only relevant simulation parameter that dictates the trend is the chosen electron mobility value of the emitter layer (Figure S10, Supporting Information). For a small μ_e, the response speed decreases with increasing voltage (Figure 6c)—as observed for the SY-OUC—whereas the trend is reversed for a high μ_e (Figure 6d). The high-mobility μ_e value of 2×10^{-5} cm² V⁻¹ s⁻¹ in the simulation corresponds to the measured value for the phosphorescent DCzPPy-Ir(ppy)₃ emitter,[43] and for the Ir-OUC we indeed find experimentally that the response speed increases when the voltage is increased (Figure 4a). One observation to note is that in the simulation the recombination zone narrows with increasing voltage and is situated closer to the QUPD-emitter interface. Thus, when μ_e is rate-limiting it takes longer for the electrons to reach the recombination zone when the voltage is increased. On the other hand, this difference in recombination zone seems to become irrelevant when μ_e of the emitter is the highest mobility in the simulation (Figure S11, Supporting Information).

We address in the simulation the observation that the 3 dB cut-off frequency for the SY-OUC decreases further during continuous device stressing (Figure 4b). We ascribe this trend to device degradation. One source of degradation in semiconducting polymer OLEDs is the formation of hole traps. Trapped charges hinder the charge transport and therefore deteriorate the bandwidth of the device.[44] Hole traps grow over orders of magnitude with operation time and dictate the long-term stability of polymer OLEDs.[45–47] If we add in the simulation emitter hole traps in sub-steps up to a concentration of 1×10^{18} cm⁻³, the 10–90% rise time increases by about 400 μs (Figure S12, Supporting Information). Furthermore, the influence of the first added hole trap fractions on the rise time is largest and the response speed levels off when more hole traps are added in the simulation. These simulation results agree with the experiment where the decrease of response speed during device stressing is largest during the first few hours (Figure 4b).

In addition to hole traps that continuously form during operation, there exists a permanently present electron trap site density in semiconducting polymers, with a number of traps of $1–3 \times 10^{17}$ cm⁻³.[48] As for the hole traps, electron traps slow down the charge transport.[49] However, for the high light intensities we experimentally used (4.9–49 mW cm⁻²) for the

light-dependent response speed measurements (Figure 4c,d), the effect of electron traps in the simulation is very small and the response speed trend does not change (Figure S13, Supporting Information). Therefore, we exclude that electron traps are the underlying reason for the observation that the response speed decreases when the light intensity is decreased.

Systematic studies on the response speed of OUCs have not been presented so far. A few reported single-parameter 3dB cut-off frequencies such as rise and fall times show that the response speed of OUCs so far is limited to around 10 kHz.[10,11,14,15] This is much lower than the response speed of organic NIR photodetectors, for which typical cut-off frequencies are well above 100 kHz.[19,35,50,51] We think that the main reason for this discrepancy is the low electric field in the emitter layer present in OUCs. This results first in a low drift velocity of electrons to the recombination zone, and second in a lower effective charge mobility value, because μ_e usually is electric field dependent and increases with increasing field ($\mu = \mu_o\exp(\gamma\sqrt{E})$, with $\gamma > 0$[52]). Another important difference between organic photodetectors and OUCs is the dependence of the response speed on the light intensity and applied voltage bias. First, for (not trap-limited[44]) organic photodetectors the response speed decreases when the light intensity is increased.[37–39] This trend is explained by a counter-voltage produced by the photocurrent. At high light intensity, this voltage is sufficiently large to lower the internal electric field which slows down the sweep-out of charges. In addition and because the drift velocity increases with the electric field, the response speed of organic photodetectors in general increases with increasing voltage bias, a feature we observe for the Ir-OUC but not for the SY-OUC.

3. Conclusions

OUCs with narrowband NIR photodetectors can be used for imaging in the presence of visible background light. This is an advantage over broadband absorber materials, where visible light absorption results in a nonselective OUC response. J-aggregated polymethine dyes are especially suited for the filter-less narrowband detection of NIR light. Here, we upconverted NIR light close to 1000 nm; however, J-aggregates of cyanine dyes with peak absorptions out to 1400 nm are known,[26] which allows imaging applications far in the shortwave infrared range. Features of the device functionality originate from the special OUC architecture and are not specific to devices with a narrowband photodetector. First, a narrow charge recombination zone situated at the interface between the electron-blocking and the emitter layer can result in substantial exciton quenching. This issue can be addressed with balanced energy levels for hole transport into the OLED or suitable interlayers between the electron-blocking and the emitter layer. The observed response speed versus light intensity trend and the result that the response speed decreases with increasing voltage can be removed in the simulation by choosing a very high electron mobility value in the emitter layer. However, it remains to be seen whether this can also be achieved experimentally. This is because our analysis suggests that the response speed of OUCs is fundamentally limited by the low drift velocity of

electrons in the emitter layer. Further studies of the factors that determine the response speed of upconversion devices are important for future applications.

4. Experimental Section

Device Fabrication: If not mentioned otherwise, TiO_2 layers (35 nm) were prepared via a sol–gel process as reported.[32] Alternatively, glass-ITO substrates were coated with TiO_2 via atomic layer deposition at a substrate temperature of 100 °C with argon as carrier gas at a base pressure of 28 Pa in a Fiji G2 system (Veeco Instruments Inc.). The precursors were tetrakis(dimethylamino)titanium(IV) (TDMAT, Sigma-Aldrich) and H_2O. TDMAT was kept at 75 °C, while H_2O was unheated. The growth rate was determined by ellipsometry on Si (100) reference substrates and linear growth was observed with a growth rate of 0.49 Å cycle^{-1}. No postdeposition annealing was performed on the TiO_2 layer, which is therefore assumed to be amorphous. Device fabrication was carried out in a glove box (H_2O < 1 ppm, O_2 < 20 ppm), except the preparation of the cyanine layer (10 nm) that was coated in ambient atmosphere. Therefore, the cyanine dye (FEW S2433) was dissolved in 2,2,2-tri-fluoroethanol (5 mg mL^{-1}) and the solution was stirred for 20 h. Then, the dye solution was spin coated without using a filter at 3000 rpm for 60 s. QUPD (Lumtec, 5 mg mL^{-1}) and the photoinitiator OPPI[53] (Sigma-Aldrich, 2.5 mg mL^{-1}) were separately dissolved in anhydrous toluene and were stirred for 30 min. Then, 1.5 wt% of OPPI was added to the QUPD solution and the film was spin coated (4000 rpm, 60 s) using a 0.45 μm filter. To promote cross-linking, films were exposed to UV-illumination (355 nm, 40 s) and annealed at 120 °C for 2 min. To realize a thicker QUPD layer (40 nm), a second film was coated on top of the first cross-linked layer. Finally, the two-layer QUPD film was rinsed with tetrahydrofuran (THF) to remove excess initiator.

NIR photodetectors were fabricated in the configuration ITO/TiO_2(35 nm)/Jcy(10 nm)/MoO_3(15 nm)/Ag(60 nm). MoO_3 (0.2 Å s^{-1}) and Ag (0.2–0.4 Å s^{-1}) were evaporated at 2×10^{-6} mbar. For Ag, a shadow mask was used defining the device area to 3.1 or 7.1 mm^2. For SY-OUCs, SY (Merck, dried at 40 °C and 0.1 mbar for 24 h) was dissoved in anhydrous toluene (5 mg mL^{-1}) and was stirred for 20 h. SY films (87 ± 6 nm) were spin coated onto QUPD at 1500 rpm for 30 s and were then annealed at 50 °C for 20 min. Ca (0.2 Å s^{-1}, 10 nm) and Al (0.2–0.4 Å s^{-1}, 70 nm) were evaporated as the top electrode. For Ir-OUCs, 26DCzPPy (TCI Chemicals, 5 mg mL^{-1}) and 10 wt% Ir(ppy)$_3$ (TCI Chemicals) were dissolved in anhydrous chlorobenzene and the solution was stirred for 30 min. The filtered (0.45 μm) blend solution was spin coated at 2500 rpm for 40 s and films (20 nm) were then annealed at 80 °C for 10 min. After that, the electron transport layer TPBi (Lumtec, 0.2–0.4 Å s^{-1}, 45 nm) and the top electrode consisting of LiF (Lumtec, 0.1 Å s^{-1}, 1 nm) and Al was evaporated.

Device Characterization: Film thicknesses were measured using an Ambios XP1 profilometer. Absorption and transmission spectra were recorded using a Varian Cary 50 Scan spectrophotometer. For the transmission spectra shown in Figure 2, air was used as the baseline. Electroluminescence spectra were measured with an integrating sphere on an Ocean Optics spectrometer QE Pro. Devices were characterized outside the glove box in a N_2-filled air-tight box covered with a glass window. EQE spectra were measured on a commercial setup (SpeQuest, ReRa solutions BV). The monochromatic light was chopped at 85 Hz during the measurement without additional bias light. Optionally, a voltage bias was applied during spectral response measurements. The responsivity R [A/W] was calculated as R = EQE/100% × λ/1240 [nm W A^{-1}], where λ is the wavelenght of the incident light in nanometer. Luminance–current–voltage characteristics were recorded using a Keithley 2400 and a Konica Minolta LS-110 luminance meter with a close-up lens 110. As the NIR light source, a 980 nm laser (Thorlabs, CPS980, 49 mW cm^{-2}) was used. In ref. [32], the experimental setup for device characterization is shown and the evaluation of the P2PCE is explained. The linear dynamic range (LDR) was calculated as LDR = 20 × log(L_{upper}/L_{lower}), where L_{upper}

and L_{lower} stand for the maximum and minimum upconverted luminance measured as a function of the NIR power density. The response speed was measured on the Paios system (Fluxim AG, Switzerland) using modulated rectangular pulses from a LED at 950 nm.

Simulation: Optical and electrical simulations were performed with Setfos 5.2 (Fluxim AG, Switzerland). The simulation procedure and the influence of individual parameter variations are presented in the Supporting Information. Energy levels for the simulations as shown in Figure 1b were taken from the literature: ITO and TiO_2,[50] QUPD,[54,55] SY,[56] 26DCzPPy,[43] Ir(ppy)$_3$,[57] and TPBi.[58] For Jcy, the HOMO value of −5.37 eV from a related heptamethine cyanine dye was adopted,[59] and the energy of the LUMO by adding the optical bandgap was obtained. Mobilites were adopted or estimated from the literature: TiO_2,[60] QUPD,[61] Jcy,[62] and μ_h(SY).[63] The Ir-OUC in detail was not simulated. However, with μ_e(TPBi) = (3.3–8) × 10^{-5} cm^2 V^{-1} s^{-1} [64] and $\mu_e = \mu_h = 2 \times 10^{-5}$ cm^2 V^{-1} s^{-1} for DCzPPy,[43] the relevant charge mobilities values of the emitter layer are much higher than for SY, which explains the different response speed versus voltage trend observed.

Conflict of Interest

The authors declare no conflict of interest.

Data Availability Statement

The data that support the findings of this study are available from the corresponding author upon reasonable request.

[1] J. Vanderspikken, W. Maes, K. Vandewal, *Adv. Funct. Mater.* **2021**, *31*, 2104060.
[2] Z. Lan, Y. S. Lau, Y. Wang, Z. Xiao, L. Ding, D. Luo, F. Zhu, *Adv. Optical Mater.* **2020**, *8*, 2001388.
[3] H. Ren, J.-D. Chen, Y.-Q. Li, J.-X. Tang, *Adv. Sci.* **2021**, *8*, 2002418.
[4] A. Armin, R. D. Jansen-van Vuuren, N. Kopidakis, P. L. Burn, P. Meredith, *Nat. Commun.* **2015**, *6*, 6343.
[5] X. Liu, Y. Lin, Y. Liao, J. Wu, Y. Zheng, *J. Mater. Chem. C* **2018**, *6*, 3499.

ADVANCED
SCIENCE NEWS

www.advancedsciencenews.com

ADVANCED
OPTICAL
MATERIALS

www.advopticalmat.de

[6] S. Zhu, R. Tian, A. L. Antaris, X. Chen, H. Dai, *Adv. Mater.* **2019**, *31*, 1900321.

[7] J. A. Carr, D. Franke, J. R. Caram, C. F. Perkinson, M. Saif, V. Askoxylakis, M. Datta, D. Fukumura, R. K. Jain, M. G. Bawendi, O. T. Bruns, *Proc. Natl. Acad. Sci. USA* **2018**, *115*, 4465.

[8] L. Gao, C. Ge, W. Li, C. Jia, K. Zeng, W. Pan, H. Wu, Y. Zhao, Y. He, J. He, Z. Zhao, G. Niu, X. Guo, F. P. G. de Arquer, E. H. Sargent, J. Tang, *Adv. Funct. Mater.* **2017**, *27*, 1702360.

[9] W. Zhou, Y. Shang, F. P. G. de Arquer, K. Xu, R. Wang, S. Luo, X. Xiao, X. Zhou, R. Huang, E. H. Sargent, Z. Ning, *Nat. Electron.* **2020**, *3*, 251.

[10] Q. Song, T. Lin, Z. Su, B. Chu, H. Yang, W. Li, C.-S. Lee, *J. Phys. Chem. Lett.* **2018**, *9*, 6818.

[11] N. Li, N. Eedugurala, D.-S. Leem, J. D. Azoulay, T. N. Ng, *Adv. Funct. Mater.* **2021**, *31*, 2100565.

[12] V. Yeddu, G. Seo, F. Cruciani, P. M. Beaujuge, D. Y. Kim, *ACS Photonics* **2019**, *6*, 2368.

[13] S.-W. Liu, C.-C. Lee, C.-H. Yuan, W.-C. Su, S.-Y. Lin, W.-C. Chang, B.-Y. Huang, C.-F. Lin, Y.-Z. Lee, T.-H. Su, K.-T. Chen, *Adv. Mater.* **2015**, *27*, 1217.

[14] X. Du, J. Han, Z. He, C. Han, X. Wang, J. Wang, Y. Jiang, S. Tao, *Adv. Mater.* **2021**, *33*, 2102812.

[15] C.-J. Shih, Y.-Z. Li, M.-Z. Li, S. Biring, B.-C. Huang, C.-W. Liu, T.-H. Yeh, D. Luo, J.-H. Lee, Y.-H. Huang, K.-T. Wong, S.-W. Liu, *Nano Energy* **2021**, *86*, 106043.

[16] R. Hany, M. Cremona, K. Strassel, *Sci. Technol. Adv. Mater.* **2019**, *20*, 497.

[17] N. Li, Z. Lan, Y. S. Lau, J. Xie, D. Zhao, F. Zhu, *Adv. Sci.* **2020**, *7*, 2000444.

[18] K. Strassel, W.-H. Hu, S. Osbild, D. Padula, D. Rentsch, S. Yakunin, Y. Shynkarenko, M. Kovalenko, F. Nüesch, R. Hany, M. Bauer, *Sci. Technol. Adv. Mater.* **2021**, *22*, 194.

[19] J. H. Kim, A. Liess, M. Stolte, A.-M. Krause, V. Stepanenko, C. Zhong, D. Bialas, F. Spano, F. Würthner, *Adv. Mater.* **2021**, *33*, 2100582.

[20] J. Han, D. Yang, D. Ma, W. Qiao, Z. Y. Wang, *Adv. Optical Mater.* **2018**, *6*, 1800038.

[21] X. Gong, M. Tong, Y. Xia, W. Cai, J. S. Moon, Y. Cao, G. Yu, C.-L. Shieh, B. Nilsson, A. J. Heeger, *Science* **2009**, *325*, 1665.

[22] B. Siegmund, A. Mischok, J. Benduhn, O. Zeika, S. Ullrich, F. Nehm, M. Böhm, D. Spoltore, H. Fröb, C. Körner, K. Leo, K. Vandewal, *Nat. Commun.* **2017**, *8*, 15421.

[23] M. Young, J. Suddard-Bangsund, T. J. Patrick, N. Pajares, C. J. Traverse, M. C. Barr, S. Y. Lunt, R. R. Lunt, *Adv. Optical Mater.* **2016**, *4*, 1028.

[24] E. D. Cosco, J. R. Caram, O. T. Bruns, D. Franke, R. A. Day, E. P. Farr, M. G. Bawendi, E. M. Sletten, *Angew. Chem., Int. Ed.* **2017**, *56*, 13126.

[25] F. Würthner, T. E. Kaiser, C. R. Saha-Möller, *Angew. Chem., Int. Ed.* **2011**, *50*, 3376.

[26] C. Sun, B. Li, M. Zhao, S. Wang, Z. Lei, L. Lu, H. Zhang, L. Feng, C. Dou, D. Yin, H. Xu, Y. Cheng, F. Zhang, *J. Am. Chem. Soc.* **2019**, *141*, 19221.

[27] J. L. Bricks, Y. L. Slominskii, I. D. Panas, A. P. Demchenko, *Methods Appl. Fluoresc.* **2018**, *6*, 012001.

[28] T. P. Osedach, A. Iacchetti, R. R. Lunt, T. L. Andrew, P. R. Brown, G. M. Akselrod, V. Bulović, *Appl. Phys. Lett.* **2012**, *101*, 113303.

[29] S. B. Anantharaman, K. Strassel, M. Diethelm, A. Gubicza, E. Hack, R. Hany, F. A. Nüesch, J. Heier, *J. Mater. Chem. C* **2019**, *7*, 14639.

[30] A. Liess, A. Arjona-Esteban, A. Kudzus, J. Albert, A.-M. Krause, A. Lv, M. Stolte, K. Meerholz, F. Würthner, *Adv. Funct. Mater.* **2018**, *29*, 1805058.

[31] J. H. Kim, T. Schembri, D. Bialas, M. Stolte, F. Würthner, *Adv. Mater.* **2021**, *33*, 2104678.

[32] K. Strassel, A. Kaiser, S. Jenatsch, A. C. Véron, S. B. Anantharaman, E. Hack, M. Diethelm, F. Nüesch, R. Aderne, C. Legnani, S. Yakunin, M. Cremona, R. Hany, *ACS Appl. Mater. Interfaces* **2018**, *10*, 11063.

[33] S. D. Yambem, M. Ullah, K. Tandy, P. L. Burn, E. B. Namdas, *Laser Photonics Rev.* **2014**, *8*, 165.

[34] M. Diethelm, Q. Grossmann, A. Schiller, E. Knapp, S. Jenatsch, M. Kawecki, F. Nüesch, R. Hany, *Adv. Optical Mater.* **2019**, *7*, 1801278.

[35] J. Huang, J. Lee, J. Vollbrecht, V. V. Brus, A. L. Dixon, D. X. Cao, Z. Zhu, Z. Du, H. Wang, K. Cho, G. C. Bazan, T.-Q. Nguyen, *Adv. Mater.* **2020**, *32*, 1906027.

[36] M. Kielar, O. Dhez, G. Pecastaings, A. Curutchet, L. Hirsch, *Sci. Rep.* **2016**, *6*, 39201.

[37] S. Ullbrich, B. Siegmund, A. Mischok, A. Hofacker, J. Benduhn, D. Spoltore, K. Vandewal, *J. Phys. Chem. Lett.* **2017**, *8*, 5621.

[38] S. Valouch, M. Nintz, S. W. Kettlitz, N. S. Christ, U. Lemmer, *IEEE Photonics Technol. Lett.* **2012**, *24*, 596.

[39] N. S. Christ, S. W. Kettlitz, S. Valouch, S. Züfle, C. Gärtner, M. Punke, U. Lemmer, *J. Appl. Phys.* **2009**, *105*, 104513.

[40] S. van Reenen, M. V. Vitorino, S. C. J. Meskers, R. A. J. Janssen, M. Kemerink, *Phys. Rev. B* **2014**, *89*, 205206.

[41] K. Sreenath, C. V. Suneesh, V. K. R. Kumar, K. R. Gopidas, *J. Org. Chem.* **2008**, *73*, 3245.

[42] M. Bauer, *Ph.D. thesis*, University Ulm (Germany) **2021**.

[43] C. Cai, S.-J. Su, T. Chiba, H. Sasabe, Y.-J. Pu, K. Nakayama, J. Kido, *Org. Electron.* **2011**, *12*, 843.

[44] F. Arca, S. F. Tedde, M. Sramek, J. Rauh, P. Lugli, O. Hayden, *Sci. Rep.* **2013**, *3*, 1324.

[45] N. B. Kotadiya, A. Mondal, P. W. M. Blom, D. Andrienko, G.-J. A. H. Wetzelaer, *Nat. Mater.* **2019**, *18*, 1182.

[46] Q. Niu, G.-J. A. H. Wetzelaer, P. W. M. Blom, N. I. Crăciun, *Adv. Electron. Mater.* **2016**, *2*, 1600103.

[47] Q. Niu, R. Rohloff, G.-J. A. H. Wetzelaer, P. W. M. Blom, N. I. Crăciun, *Nat. Mater.* **2018**, *17*, 557.

[48] H. T. Nicolai, M. Kuik, G. A. H. Wetzelaer, B. de Boer, C. Campbell, C. Risko, J. L. Brédas, P. W. M. Blom, *Nat. Mater.* **2012**, *11*, 882.

[49] M. Kuik, G.-J. A. H. Wetzelaer, H. T. Nicolai, N. I. Craciun, D. M. De Leeuw, P. W. M. Blom, *Adv. Mater.* **2014**, *26*, 512.

[50] H. Zhang, S. Jenatsch, J. De Jonghe, F. Nüesch, R. Steim, A. C. Véron, R. Hany, *Sci. Rep.* **2015**, *5*, 9439.

[51] Y. Yao, Y. Liang, V. Shrotriya, S. Xiao, L. Yu, Y. Yang, *Adv. Mater.* **2007**, *19*, 3979.

[52] L. Bozano, S. A. Carter, J. C. Scott, G. G. Malliaras, P. J. Brock, *Appl. Phys. Lett.* **1999**, *74*, 1132.

[53] K. Strassel, S. P. Ramanandan, S. Abdolhosseinzadeh, M. Diethelm, F. Nüesch, R. Hany, *ACS Appl. Mater. Interfaces* **2019**, *11*, 23428.

[54] K.-W. Tsai, M.-K. Hung, Y.-H. Mao, S.-A. Chen, *Adv. Funct. Mater.* **2019**, *29*, 1901025.

[55] X. Yang, D. C. Müller, D. Neher, K. Meerholz, *Adv. Mater.* **2006**, *18*, 948.

[56] M. Zhang, S. Höfle, J. Czolk, A. Mertens, A. Colsmann, *Nanoscale* **2015**, *7*, 20009.

[57] M. Ikai, S. Tokito, Y. Sakamoto, T. Suzuki, Y. Taga, *Appl. Phys. Lett.* **2001**, *79*, 156.

[58] S.-C. Lo, N. A. H. Male, J. P. J. Markham, S. W. Magennis, P. L. Burn, O. V. Salata, I. D. W. Samuel, *Adv. Mater.* **2002**, *14*, 975.

[59] A. C. Véron, H. Zhang, A. Linden, F. Nüesch, J. Heier, R. Hany, T. Geiger, *Org. Lett.* **2014**, *16*, 1044.

[60] P. Tiwana, P. Docampo, M. B. Johnston, H. J. Snaith, L. M. Herz, *ACS Nano* **2011**, *5*, 5158.

[61] H.-J. Jhuo, P.-N. Yeh, S.-H. Liao, Y.-L. Li, S. Sharma, S.-A. Chen, *J. Mater. Chem. A* **2015**, *3*, 9291.

[62] L. Wang, S. Jenatsch, B. Ruhstaller, C. Hinderling, D. Gesevičius, R. Hany, F. Nüesch, *Adv. Funct. Mater.* **2018**, *28*, 1705724.

[63] H. Najafov, I. Biaggio, T.-K. Chuang, M. K. Hatalis, *Phys. Rev. B* **2006**, *73*, 125202.

[64] W.-Y. Hung, T.-H. Ke, Y.-T. Lin, C.-C. Wu, T.-H. Hung, T.-C. Chao, K.-T. Wong, C.-I. Wu, *Appl. Phys. Lett.* **2006**, *88*, 064102.